

**RASTER MAPS OF CRATERS DEPTHS IN SOUTHERN HEMISPHERE OF MARS: POTENTIAL PROXY FOR SPATIAL DISTRIBUTION OF GROUND ICE.** Tomasz. F. Stepinski<sup>1</sup> and Erik R. Urbach<sup>1</sup>,  
<sup>1</sup>Lunar and Planetary Institute, 3600 Bay Area Blvd., Houston, TX 77058, USA. (tom@lpi.usra.edu, urbach@lpi.usra.edu).

**Abstract.** Raster maps of relative crater depths are constructed for the southern hemisphere of Mars using data from > 45,000 craters detected and measured by a computer algorithm. These maps show a striking spatial pattern that we interpret in terms of spatial variations of the depth to the upper boundary of the cryosphere. Such interpretation indicates hemisphere-wide existence of shallower ground ice southward of ~ 40°S.

**Introduction.** It is widely believed that a significant quantity of water resides in Martian subsurface in the form of ground ice. As the ground ice is not directly observable on global scale (a situation that may change with more data from ground penetrating radars), we have to rely on surface expressions of ground ice for determining its presence. In particular morphology of impact craters, such as the existence of rampart ejecta [1,2] or their “softened” appearance [3], is often used to infer presence of ground ice. Such morphologic evidence was obtained in the past on the basis of visual inspection of limited number of images. In [4] it was demonstrated that visual differences between softened and unsoftened craters can be quantified by measuring several crater parameters, and in particular the depth-to-diameter ratio ( $d/D$ ). Thus, mapping spatial variability of ( $d/D$ ) constitutes a plausible method for objective determination of spatial distribution of ground ice.

Recently we have developed [5,6] a robust crater detection algorithm (CDA) capable of identifying and characterizing virtually all craters in a given site having diameter  $D \geq 3$  km. We have applied this CDA to the entire southern hemisphere of Mars. Our algorithm has identified 45,556 craters and estimated their diameters ( $D$ ) and depths ( $d$ ). This crater dataset is used to construct raster maps of depth-to-diameter ratio ( $d/D$ ) for craters in different size bins. Such maps are used to infer spatial distribution and properties of ground ice.

**Methods.** Our CDA is a two stage system that uses topography data as given by the MOLA Mission Experiment Gridded Data Record (MEGDR) [7] with resolution of 1/128 degree. The details of the CDA are given in [5,6]. Its application to the entire hemisphere requires subdividing the hemisphere into overlapping tiles having size 15° by 15°. The craters are identified and measured at each tile separately and the results from individual tiles are concatenated into a single

catalog from which duplicate detections are eliminated.

Identified craters are divided into six size bins,  $D < 5$  km,  $5 \text{ km} \leq D < 10$  km,  $10 \text{ km} \leq D < 15$  km,  $15 \text{ km} \leq D < 20$  km,  $20 \text{ km} \leq D < 25$  km,  $D \geq 25$  km. Using craters from each bin separately, raster maps of ( $d/D$ ) are constructed using moving average technique.

**Results.** Fig.1 shows the raster maps of ( $d/D$ ) for all six crater size bins. The maps are shown in the Lambert azimuthal equal-area projection centered on the south pole and reveal existence of three different types of spatial patterns. (1) For craters with  $D < 10$  km (the first two size bins) there is a clear concentric pattern. The hemisphere is divided into two zones, the outer, zone ( $Zone_E$ , shown in reds) extending from the equator (the perimeter of the map) to the latitude of up to 40°S, and the inner, zone ( $Zone_{HL}$ ), shown in yellows) extending from to the latitude of ~ 40°S to the south pole (center of the map). In  $Zone_E$  the craters are relatively deep, whereas in  $Zone_{HL}$  the craters are relatively shallow. There is little longitudinal variation in ( $d/D$ ) values. (2) For craters with  $D > 25$  km (the sixth size bin) there is no spatial pattern on the hemispheric scale, although some longitudinal variation in the values of ( $d/D$ ) is observed. Throughout most parts of the hemisphere the craters of these sizes have the same, low values of relative depths. (3) For  $10 \text{ km} < D < 25$  km craters (the third to fifth size bins) the concentric pattern, so pronounced for craters in the smaller size bins, is progressively weaker and the maps start to show some longitudinal variations.

**Discussion.** The patterns on Fig. 1 are consistent with earlier observations [8], although they reflect the existing spatial variations of craters morphology in the most complete fashion due to a large number of data used. Two interpretations have been offered to explain the pattern: (a) mantling [8], (b) viscous relaxation of craters due to existence of ground ice [9]. The detailed comparison of these two hypothesis is beyond the scope of this paper. Here we concentrate on demonstrating that the set of patterns observed on Fig. 1 can be explained by an existence of the cryosphere with the depth of its upper boundary ( $z_0$ ) significantly lowered in the equatorial regions, just as predicted by models based on ice stability concept [10,11,12]. Calculations [9,13,14] of viscous relaxation indicate that the style of crater modification depends on the  $z_1/D$  ratio, where  $z_1$  is the depth of the lower boundary.

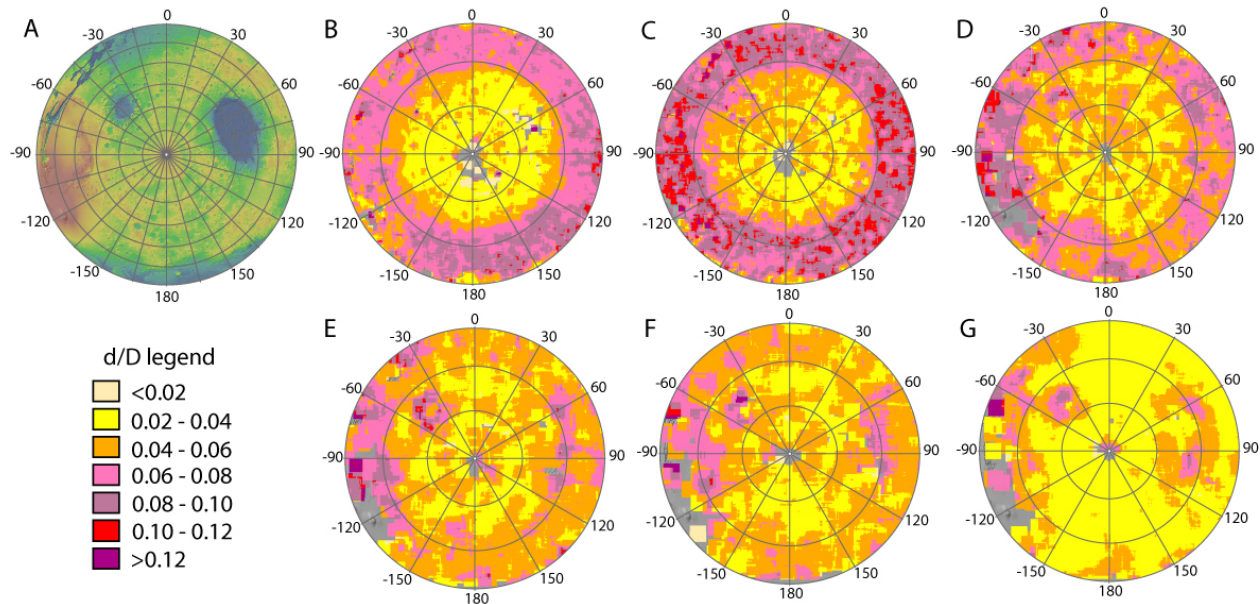


**Figure 1.** Raster maps of spatial distribution of  $(d/D)$  in the southern hemisphere of Mars. All maps are shown in the Lambert azimuthal equal-area projection centered on the south pole. (A) The topographic map of the southern hemisphere is shown for reference. (B) - (G) Maps of  $(d/D)$  constructed for craters  $D < 5$  km,  $5 \text{ km} \leq D < 10$  km,  $10 \text{ km} \leq D < 15$  km,  $15 \text{ km} \leq D < 20$  km,  $20 \text{ km} \leq D < 25$  km,  $D \geq 25$  km, respectively. Different colors correspond to different values of  $(d/D)$  as shown in the legend. Pixels that lacks sufficient number of craters in their neighborhood to calculate moving average are shown in gray.

of the cryosphere. For  $z_1/D > (z_1/D)^*$ , corresponding to a crater placed in a cryosphere that is deep relative to the crater size, the dominant modification effect is raising of the crater floor resulting in significant decrease of crater's  $(d/D)$  value. For  $z_1/D < (z_1/D)^*$ , corresponding to a crater placed in a cryosphere that is shallow relative to the crater size, there is no significant modification of crater's  $(d/D)$  value. The threshold value is  $(z_1/D)^* \sim 1/(2\pi) \approx 0.16$ .

Spatial patterns seen on Fig. 1 are consistent with the viscous relaxation model, and provide numerical constrains on the shape and the character the cryosphere. First, the concentric pattern observed for craters with  $D < 10$  km constrains the location of  $z_0$ . In  $Zone_E$  the high values of  $(d/D)$  indicate absence of viscous relaxation. Thus  $z_0$  must be located deeper than the depth of 10-km-size craters located in the  $Zone_E$ , or  $z_0 \geq 0.9$  km. In  $Zone_{HL}$  the craters are characterized by low values of  $(d/D)$  indicating presence of viscous relaxation in the  $z_1/D > (z_1/D)^*$  regime and thus  $z_0 \approx 0$ . According to this interpretation the boundary between the shallow and deep ground ice follows the red-yellow contact line on Fig. 1 (panels B and C). This boundary is located between  $30^\circ\text{S}$ . and  $40^\circ\text{S}$  and it depends only weakly on longitude. Second, the lack of spatial variability in  $(d/D)$  for craters with  $D \geq 25$

km constrains the location of  $z_1$ . The similarity of  $(d/D)$  values for craters located in  $Zone_E$  and  $Zone_{HL}$ , despite the absence of ground ice in the top 0.9 km within the  $Zone_E$ , points to a  $z_1/D < (z_1/D)^*$  regime in both zones. This leads to an estimate of the lower boundary of the cryosphere:  $z_1 \leq 0.16 \cdot 25 \text{ km} \sim 4$  km.

**References:** [1] Costard, F. M. (1989) *Earth, Moon, and Planets*, 45, 265-290. [2] Kuzmin, R. O. et al. (1989) *Solar System Research*, 22(3). [3] Squyers, S. W. and Carr M. H. (1986) *Science*, 231, [4] Jankowski, D. G. and Squyers, S. W. (1992) *Icarus* 100, 26-39. [5] Stepinski, T. F. et al. (2007) *LPS XXXVIII*, Abstract #1338. [6] Stepinski, T.F. et al. (2007) *Icarus*, submitted. [7] Smith D. et al. (2003) NASA Planetary Data System, MSG-M-MOLA-5-MEGDR-L3-V1.0. [8] Soderblom, L.A. et al. (1973), *J. Geophys. Res.* 78(20), 4117-4122. [9] Parmentier, E. M. and Head, J. W. (1981) *Icarus*, 47, 100-111. [10] Clifford S. M. and Hillel D. (1983) *JGR*, 88, 2456-2474. [11] Fanale F. P. et al. (1986) *Icarus*, 67, 1-18. [12] Clifford S. M. (1993) *JGR*, 98 E6, 10,973-11,016., 121-133. [13] Jankowski, D. G. and Squyers, S. W. (1993) *Icarus*, 106, 365-379. [14] Pathare, A. V. et al. (2005) *Icarus* 174, 396-418.